Assembly and Mechanical Properties of the Cargo-Free and Cargo-Loaded Bacterial Nanocompartment Encapsulin

Joost Snijder,[†,‡,§] Olga Kononova,[‖,#] Ioana M. Barbu,[†,‡] Charlotte Uetrecht,[†,‡] W. Frederik Rurup,[○] Rebecca J. Burnley,[†,‡] Melissa S. T. Koay,[○] Jeroen J. L. M. Cornelissen,[○] Wouter H. Roos,[§,□] Valeri Barsegov,[‖,#] Gijs J. L. Wuite,*[,§] and Albert J. R. Heck*[,†,‡]

[†]Biomolecular Mass Spectrometry and Proteomics, Bijvoet Center for Biomolecular Research and Utrecht Institute for Pharmaceutical Sciences, Utrecht University, Padualaan 8, 3584 CH, Utrecht, The Netherlands

[‡]Netherlands Proteomics Centre, Padualaan 8, 3584 CH, Utrecht, The Netherlands

[§]Natuur- en Sterrenkunde and LaserLab, Vrije Universiteit, De Boelelaan 1081, Amsterdam, The Netherlands

[‖]Department of Chemistry, University of Massachusetts, Lowell, Massachusetts 01854, United States

[#]Moscow Institute of Physics and Technology, Moscow Region, Russia 141700

[○]Department of Biomolecular Nanotechnology, MESA+ Institute, University of Twente, P.O. Box 217, 7500 AE Enschede, The Netherlands

[□]Moleculaire Biofysica, Zernike instituut, Rijksuniversiteit Groningen, Nijenborgh 4, 9747 AG Groningen, The Netherlands

ⓢ *Supporting Information*

ABSTRACT: Prokaryotes mostly lack membranous compartments that are typical of eukaryotic cells, but instead, they have various protein-based organelles. These include bacterial microcompartments like the carboxysome and the virus-like nanocompartment encapsulin. Encapsulins have an adaptable mechanism for enzyme packaging, which makes it an attractive platform to carry a foreign protein cargo. Here we investigate the assembly pathways and mechanical properties of the cargo-free and cargo-loaded nanocompartments, using a combination of native mass spectrometry, atomic force microscopy and multiscale computational molecular modeling. We show that encapsulin dimers assemble into rigid single-enzyme bacterial containers. Moreover, we demonstrate that cargo encapsulation has a mechanical impact on the shell. The structural similarity of encapsulins to virus capsids is reflected in their mechanical properties. With these robust mechanical properties encapsulins provide a suitable platform for the development of nanotechnological applications.
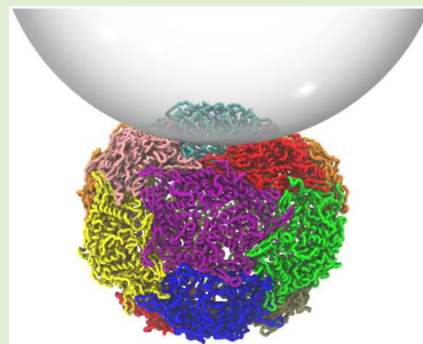
Cells have many compartments, which allow many incompatible biochemical reactions to take place simultaneously within the crowded environment of the cell. Compartments may act as protective selectivity barriers, sequestering toxic reaction products or conversely protecting labile products from degradation by enzymes from outside of the compartment. Moreover, local concentrations, pH and redox potential inside compartments have a strong impact on reaction kinetics. Such concepts are also exploited in chemical engineering through the use of various types of chemical reactors. Creation of such nanoscale reactors may become of particular importance to further developments in nanotechnology. Inspiration has been taken from naturally occurring nanocompartments in this regard.[1] Most notably, the use of engineered ferritin cages and virus capsids has led to the development of various protein-based nanoreactors, nanocarriers for drug delivery and contrast agents for bioimaging applications.[2−6]

Prokaryotic cells typically lack the membranous compartments characteristic of eukaryotes, but contain a variety of protein-based compartments instead.[7] Bacterial microcompartments (BMC) such as the carboxysome represent a notable class of protein-based organelles in prokaryotes.[8−10] They are strongly faceted hollow protein shells that package the enzymes of an entire metabolic pathway in the shell interior. Moreover, bacterial nanocompartments called encapsulins have been discovered recently.[11−14] The structure of the encapsulin protein subunit has the HK97-fold, which is typical for many bacteriophage capsids. Encapsulins are icosahedral shells, thus, forming a virus-like capsid, albeit of prokaryotic rather than viral origin. Encapsulin packages an enzyme in vivo that is targeted to the shell interior via a specific C-terminal anchoring sequence on the cargo protein. Interestingly, this mechanism
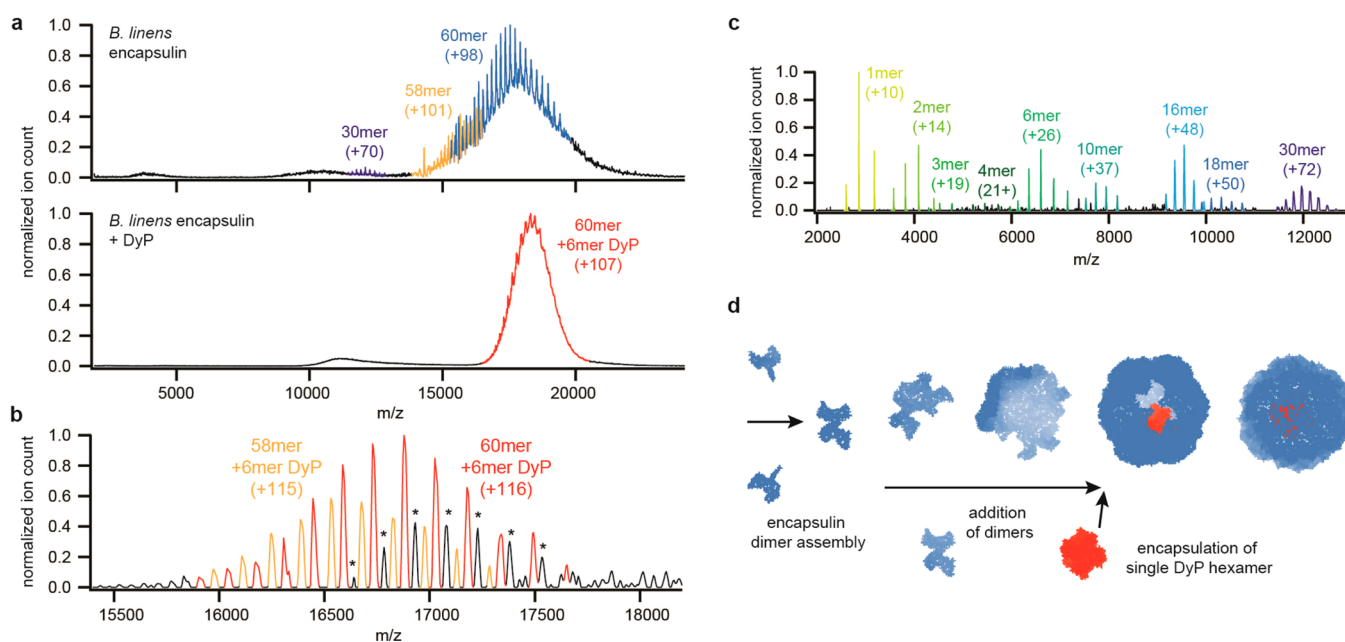
Figure 1. Native MS reveals that *B. linens* encapsulin packages a single copy of DyP. (a) Native MS TOF spectra of recombinant encapsulin expressed alone or together with DyP. Assigned complexes are highlighted in color, main charge states are indicated in parentheses. (b) Native MS Orbitrap spectrum of encapsulin coexpressed with DyP. The asterisks indicate an unassigned complex. (c) Native MS Orbitrap spectrum of lower mass-to-charge region of encapsulin coexpressed with DyP. All experimental masses are listed in SI, Table S1. (d) Schematic impression of proposed assembly pathway of *B. linens* encapsulin.

for cargo encapsulation is adaptable to non-native molecules by fusing the C-terminus of the desired cargo with the encapsulin anchoring sequence genetically,[15−17] making encapsulin an attractive platform for engineered nanoreactors and nano-carriers.

Notwithstanding their potential use in nanotechnology, little is known about the process of enzyme encapsulation in these bacterial nanocompartments. In particular, it is not known how many copies of the cargo enzyme are packaged in the shell interior or how cargo encapsulation affects the material properties of the shell. Here, we combine native mass spectrometry (MS), atomic force microscopy (AFM), and a multiscale molecular modeling approach to nanoindentation in silico to explore, for the first time, the assembly and mechanical properties of the cargo-free and cargo-loaded nanocompart-ment encapsulin from *Brevibacterium linens* and *Thermotoga maritima*. We show that *B. linens* encapsulin packages a single copy of the hexameric cargo enzyme DyP, and we provide evidence that formation of the shell occurs by the addition of dimers of the encapsulin subunit. The application of compressive force using AFM nanoindentation reveals that the capsid-like nanocompartment exhibits a stiff mechanical response, similar to structurally related bacteriophage capsids. Cargo loading has a destabilizing effect on the nanocompart-ment. Nanoindentation in silico allowed us to uncover the structural changes and resolve the thermodynamic state functions that govern the response of encapsulin to external mechanical factors. Taken together, our results provide valuable insight into the mechanism of deformation and structural collapse of biologically inspired nanocompartments and demonstrate that encapsulin is a mechanically rigid single-enzyme nanoreactor, reaffirming its great potential for the design of robust engineered nanodevices.

■ MATERIALS AND METHODS

Sample Preparation. Empty and DyP or TFP-filled encapsulin were expressed in *E. coli* cells and purified using previously described procedures.[14,15,39]

Native Mass Spectrometry. Samples were buffer exchanged to 100−200 mM ammonium acetate pH 6.8 with five rounds of concentration-dilution, using Vivaspin 500 10 kDa MWCO centrifugal filter units. Aliquots of 1−2 μL, at a final concentration of 5−10 μM, were loaded into gold-coated borosilicate capillaries (prepared in-house) for nanoelectrospray ionization. Samples were analyzed on a QToF II instrument that was modified for optimal transmission of large ions.[40] The source pressure was set at 10 mbar, collision cell pressure at 1.5×10^{-2} mbar, using xenon as collision gas.[41,42] Capillary voltage was set at 1300−1500 V, and the sample cone voltage was set at 160 V. Higher mass ions were analyzed at a collision voltage of 100 V and the lower mass ions at 30−60 V. Additional measurements were performed on an Exactive plus EMR, modified for transmission of higher m/z ions.[19,20] Capillary voltage was set at 1200 V, and source fragmentation was set at 30 V. HCD collision voltage was set at 70 V, using xenon as collision gas. Spectra were acquired at a transient time of 32 ms using the transient averaging function.

Atomic Force Microscopy. Encapsulin samples were prepared in 20 mM Tris pH 7.4, 20 mM magnesium dichloride, and 150 mM sodium chloride, at a final concentration of 0.5−1 μM. We used silanized glass slides as substrates for AFM imaging and nano-indentation. The glass slides were prepared by cleaning them in a saturated solution of potassium hydroxide in 90% ethanol, followed by thorough rinsing with Milli-Q water, drying, and overnight incubation in a hexamethyl disilazane vapor, as previously described.[30] A droplet of 100 μL of the encapsulin solution was incubated for 30 min on a glass slide, after which another 100 μL of buffer was added. We used Olympus OMCL-RC800PSA rectangular, silicon-nitride cantilevers with a nominal spring constant of 0.05 N/m and a nominal tip radius of 15 nm. Cantilevers were calibrated using the method of Sader et al.,[43] giving an average value of 0.0527 N/m. Measurements were performed with a Nanotec electronica AFM in jumping mode.[44] Imaging was performed with an average maximum imaging force of approximately 30−50 pN. Nanoindentation was performed with a probe velocity of 30 nm/s, unless stated.[43] Fatigue experiments were

performed by placing the tip 35 nm above the substrate and performing repeated approach−retraction cycles of 20−30 nm, which resulted in a maximum force of 0.2−0.3 nN on the nanocompartment. AFM images were analyzed with WSxM software,[45] and nano-indentation data was analyzed using a previously described home-built LabView application.[32]

Nanoindentations In Silico and Theoretical Interpretation of Force−Indentation Spectra. Dynamic force measurements in silico were performed using the Self Organized Polymer based modeling[34−36] and GPU-accelerated Langevin simulations with inclusion of hydrodynamic interactions between amino acid residues[33,37,46] (see Supporting Information (SI)). We used the structure of encapsulin shell obtained performing 30 ns all-atom MD simulations at equilibrium. The SOP model of encapsulin was parametrized as described in Supplementary Methods, SI. We used a spherical tip of radius R_{tip} = 20 nm to compress the shell along the 2-, 3-, and 5-fold symmetry axes. The tip−shell interactions were described by the repulsive Lennard-Jones potential $V_{tip} = \sum_i \varepsilon_{tip}(\sigma_{tip}/(|r_i - r_{tip}| - R_{tip}))^6$, where r_i is the ith particle coordinate, ε_{tip} = 4.18 kJ/mol, and σ_{tip} = 1.0 Å. To prevent the encapsulin shell from sliding and rolling, we constrained six $C\alpha$-atoms at the shell bottom to a virtual mica surface. To mimic the experimental force measurements, the tip exerted the time-dependent force $f = f(t)n$ in the direction n perpendicular to the outer shell surface. The force magnitude $f(t) = r_f t$ increased linearly in time t with the force-loading rate $r_f = \kappa v_f$ (v_f = 1.0 μm/s is the probe velocity and κ = 0.05 N/m is the cantilever spring constant). The resisting force (F) from the encapsulin shell, which corresponds to the experimentally measured indentation force, was calculated using the energy output from simulations. In nanomanipulations in silico, we controlled the piezo displacement Z (cantilever base) and the cantilever tip position X. Calculation of the thermodynamic quantities and theoretical modeling of the experimental and simulated FX spectra was performed using the simulation output as described in the Supporting Information.

■ RESULTS

Encapsulin Assembles by the Addition of Dimers and Packages a Single Copy of the Cargo Enzyme. The encapsulin nanocompartment from *B. linens* is a *T* = 1 icosahedral shell that packages a hexameric enzyme, known as a dye-decolorizing peroxidase (DyP).[14] The inner volume of the icosahedral shell far exceeds the volume of the DyP hexamer, but the shape and positioning of the cargo may pose restrictions on the maximum number of hexamers that can be accommodated within an encapsulin nanocompartment. It is therefore not known or self-evident how many copies of DyP are packaged in one compartment. Here, we determined the number of DyP hexamers in encapsulin shells by native MS, a technique that allows the mass of the intact nanocompartments to be measured with a precision below 1 kDa.[18] When the *B. linens* encapsulin subunit is recombinantly expressed in the absence of DyP, the main component we detect by native MS has a mass of 1718.2 ± 0.3 kDa, corresponding to the cargo-free compartment consisting of 60 copies of encapsulin with an expected mass of 1715.6 kDa (see Figure 1a and Supporting Information, Table S1). In addition to the complete compartment, we also detect a substantial population with a mass of 1660.6 ± 0.5 kDa, corresponding to a 58mer of the encapsulin subunit (expected mass of 1658.8 kDa), as well as a smaller component of 860.0 ± 0.3 kDa, corresponding to 30 copies of the subunit (expected mass of 857.8 kDa). When the encapsulin subunit is coexpressed with DyP, we detect a more narrowly distributed signal, presumably because specific cargo loading excludes random components from the expression system to become encapsulated. The spectrum appears rather crowded, but a single series of charge states can

still be resolved. The mass of this main component is determined at 1966.0 ± 0.3 kDa, corresponding to 60 copies of the encapsulin subunit and 1 copy of the DyP hexamer (expected mass 1957.2 kDa, stable formation of DyP hexamers was also confirmed by native MS in a separate experiment, see SI, Figure S1). Encapsulin thus seems to package a single enzyme, exclusively. To confirm our assignments we also analyzed this sample on an Orbitrap modified for native MS of megadalton protein complexes.[19,20] This instrument provides higher resolution compared to the modified time-of-flight instrument, allowing a more definitive assessment of whether other stoichiometries of encapsulin-DyP are present. The main component detected on the Orbitrap instrument exhibits a mass of 1957.8 ± 0.5 kDa, corresponding closely to the expected mass of the complete nanocompartment with one DyP hexamer (see Figure 1b). Another minor component that is also detected is 1901.0 ± 0.2 kDa, corresponding to 58mer encapsulin with one hexameric DyP (expected mass of 1900.0 kDa). The analysis on the Orbitrap instrument thus confirmed that encapsulin exclusively packages a single copy of the DyP hexamer and additionally revealed the presence of incomplete shells with encapsulated cargo.

Both cargo-free and DyP-loaded 58mers of encapsulin are detected in the native MS experiments, showing that assembly of the nanocompartment can be incomplete. Simulations of capsid assembly have consistently indicated that late assembly intermediates can be especially long-lived.[21,22] The detection of 58mer complexes of encapsulin by native MS provides experimental evidence for the existence of these late-intermediates in capsid assembly.[23] As it is not clear whether the observed 58mer complexes are true assembly intermediates on-pathway to completion, they may alternatively represent an early dissociation product of encapsulin. The incomplete shells lack a dimer of the encapsulin subunit, suggesting that the dimer is a stable substructure of encapsulin, which may be the unit of assembly of the nanocompartment. We also analyzed the lower mass-to-charge region of the encapsulin samples in more detail, revealing a range of additional smaller subcomplexes of encapsulin, ranging up to 30mers (see Figure 1c). Note that all subcomplexes, including the 58mer, are detected with a number of charges that is consistent with their origin in solution, following the expected trend for nano-electrospray ionization of intact noncovalent protein complexes, which excludes the possibility that they could originate as products of dissociation in the gas-phase. The detected subcomplexes show a distinct preference for even numbers of encapsulin subunits. This further supports the notion that the dimer represents a stable substructure of encapsulin and suggests that the nanocompartment assembles by the addition of dimers. When the crystal structure of *T. maritima* encapsulin was initially reported, it was noted that it displays particularly strong interactions across the 2-fold icosahedral symmetry axis of the shell, owing to the extended E-loop of the subunits.[14] We therefore propose an assembly pathway of encapsulin whereby dimers grow toward a complete nanocompartment by the addition of yet more 2-fold symmetry related dimers, encapsulating a single DyP hexamer in the process (see Figure 1d).

Cargo Loading has a Destabilizing Effect on Encapsulin Nanocompartments. Virus capsids, especially those of bacteriophages, are particularly attractive platforms to build nanoreactors as they can withstand internal pressures of 10−100 atm and have the rigidity of hard plastics.[24−29] The
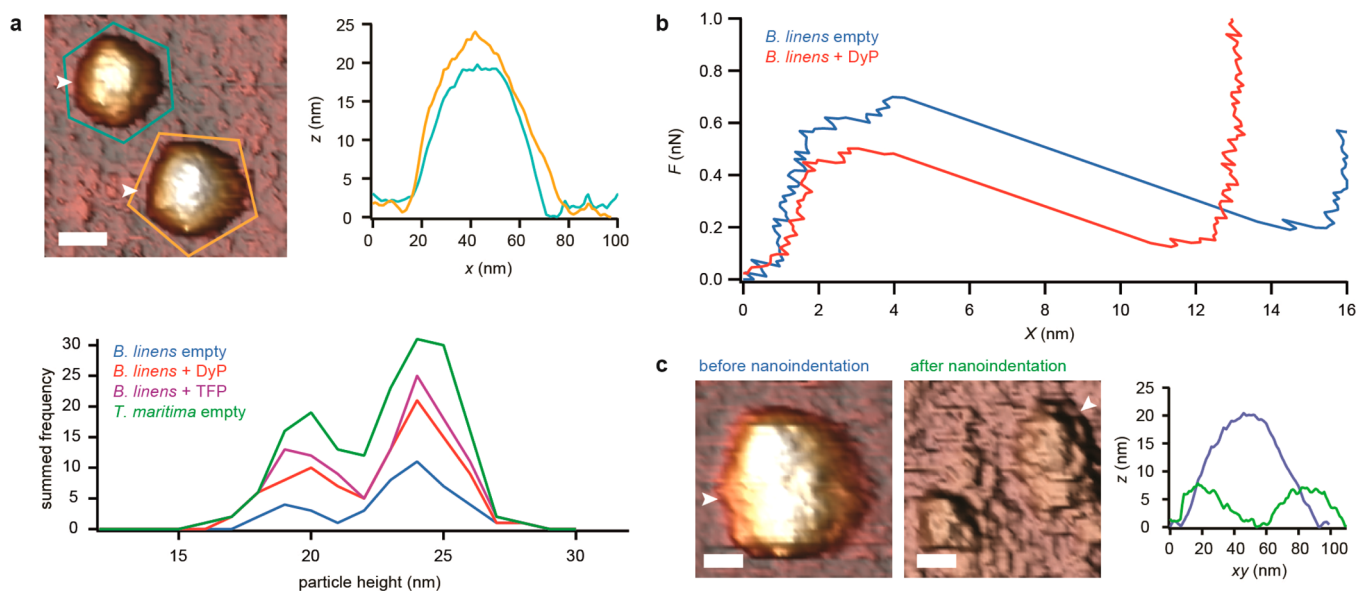
Figure 2. AFM indentation of encapsulin nanocompartments. (a) AFM image of *B. linens* encapsulins with DyP cargo, showing the two typical particle heights. Scale bar is 30 nm; image is colored according to height, from dark brown (0 nm) to white (25 nm). White arrowheads indicate the trajectory of the corresponding height profiles. Bottom panel shows the cumulative height distributions of all tested samples. The green and yellow polygons circumscribe particles that are presumably oriented by 2/3-fold and 5-fold icosahedral symmetry, respectively. (b) Typical FX curves for DyP-free and DyP-loaded encapsulin, as indicated. (c) AFM images of DyP-free encapsulin nanocompartment before and after indentation. Scale bars are 20 nm; white arrowheads indicate the trajectory of the corresponding height profiles.

Table 1. Nanoindentation of Encapsulins[a]

sample info			k (N/m)		F^* (nN)		X^* (nm)		
species	type	probe velocity (nm/s)	avg	SEM	avg	SEM	avg	SEM	n
B. linens	cargo-free	30	0.27	0.02	0.64	0.04	3.0	0.3	46
		1000	0.36	0.01	0.82	0.05	2.8	0.3	22
	DyP-loaded	30	0.25	0.02	0.44	0.03	2.7	0.2	54
	TFP-loaded	30	0.24	0.01	0.42	0.04	3.1	0.5	26
T. maritima	cargo-free	30	0.25	0.02	0.63	0.03	3.5	0.3	56

[a]Average (avg) and standard error of the mean (SEM) of spring constant (k), critical breaking force (F^*), critical indentation (X^*), and number of particles (n).

mechanical properties of virus capsids have been investigated using atomic force microscopy (AFM) nanoindentation experiments.[30,31] Whether bacterial nanocompartments like encapsulin are similarly rigid and robust is not known. Figure 2a shows an AFM image of encapsulin particles, illustrating the range of different shapes of the nanocompartment. Most notably, the particles vary in apparent height. The differences correlate with possible orientations of the particle on the glass substrate: the ~20 nm particle would be deposited on the 2-/3-fold symmetry axis, whereas the ~24 nm particle would be deposited on the 5-fold axis. The orientation of the particles could not be unambiguously determined in most cases, but the bimodal height distribution was consistently observed.

Two typical force−indentation (FX) curves obtained for DyP-free and DyP-loaded *B. linens* encapsulins are displayed in Figure 2b. The FX curves show the initial weakly nonlinear response for $X \approx 0-2$ nm for both the DyP-free and DyP-loaded shell, followed by a more linear response for $X \approx 1-4$ nm before the mechanical failure of the shell, which occurs at the critical indentation $X^* \approx 3-4$ nm and critical force $F^* \approx 0.64 \pm 0.04$ nN for the DyP-free encapsulin, and $X^* \approx 2-3$ nm and $F^* \approx 0.44 \pm 0.03$ nN for the DyP-loaded encapsulin (see Table 1). AFM imaging of encapsulin before and indentation reveals the collapsed debris of the shell after

mechanical failure (Figure 2c). From the linear-like region of the FX curve, the spring constant k_{enc} can be extracted, which characterizes the strength of elastic response of the particle. The obtained values of k_{enc} for the DyP-free *B. linens* encapsulin are $k_{enc} \approx 0.27 \pm 0.02$ N/m; for the DyP-loaded compartment $k_{enc} \approx 0.25 \pm 0.02$ N/m (see Table 1). This quantity, as well as critical force F^* and critical indentation X^* weakly depend on the force-loading rate, controlled by adjusting the probe velocity (see Table 1).[32] Comparing DyP-free and DyP-loaded compartments, we observe no significant effect of cargo encapsulation on the spring constant of the shell and critical indentation. However, the cargo encapsulation significantly decreases the value of critical force F^*, implying that the cargo-loaded shell becomes less stable. The same effect was observed in nanocompartments with a non-native cargo that binds with the same anchoring sequence as DyP (Teal Fluorescent Protein, TFP-loaded, see Table 1). This suggests that the drop in breaking force is caused specifically by binding of the cargo anchoring sequence. DyP loading also makes the nanocompartment more sensitive to material fatigue observed in a course of repeated forced indentation measurements (see SI, Figure S2).

Encapsulin Provides a Mechanically Rigid and Resilient Biomaterial. The AFM nanoindentation experi-
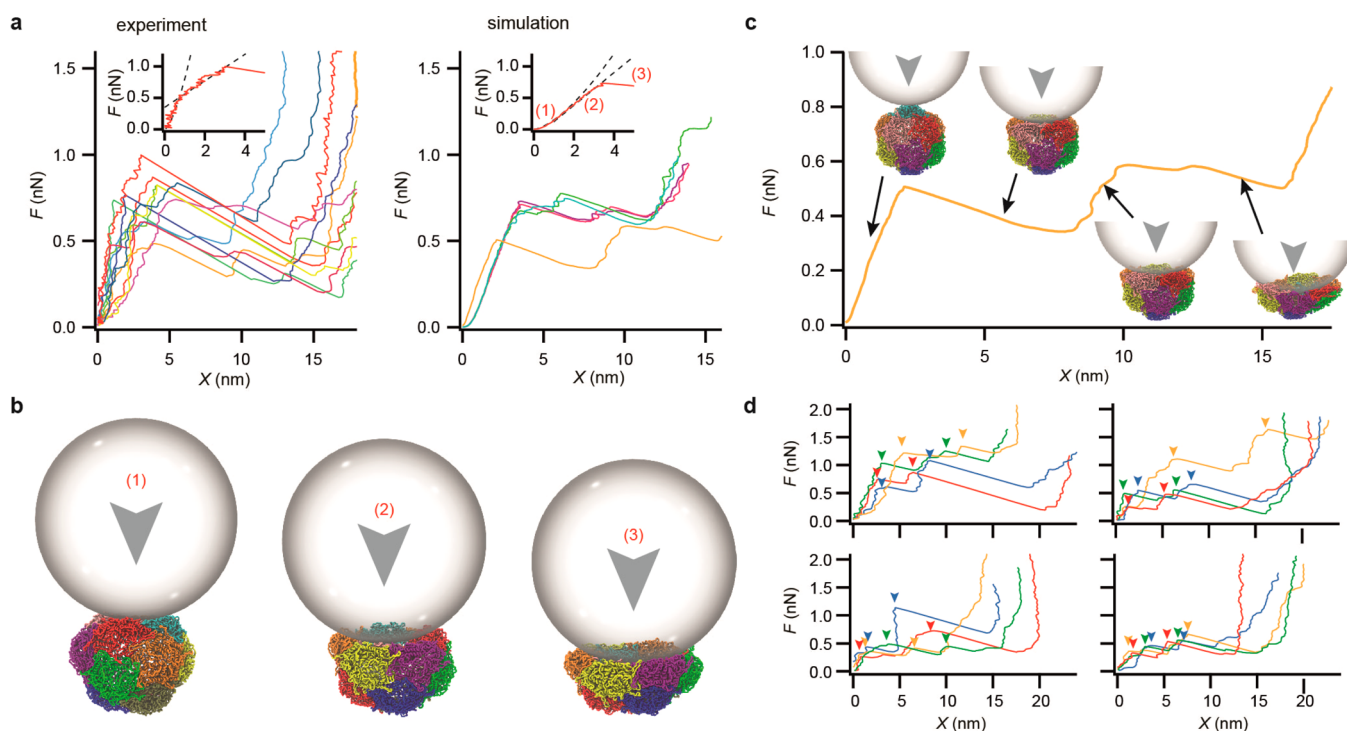
Figure 3. Dynamic structural transitions in cargo-free *T. maritima* encapsulin from nanoindentations in vitro and in silico. (a) Experimental and simulated FX curves. Typical experimental curves are shown in arbitrary colors. The insets magnify the FX curves to illustrate the initial nonlinear (Hertzian) regime of deformation followed by the linear force response. The numbers in parentheses refer to the snapshots shown in panel b. The simulated curves correspond to the 2-fold orientation (green-blue), 3-fold orientation (magenta-red), and 5-fold orientation (yellow-orange). (b) Snapshots from in silico nanoindentations along the 3-fold symmetry axis, showing the initial compression of the protein layer under the tip and subsequent bending of side portions of the capsid, which result in the global structural collapse of the shell. (c) An FX curve from in silico nanoindentation along the 5-fold symmetry axis. Snapshots illustrate buckling of the vertex (first force peak), which is followed by continuous indentation and structural collapse of the shell (second force peak). (d) Experimental FX curves displayed in arbitrary colors showing the two-step transitions (colored arrowheads indicate peak forces). Curves represent particles from all tested encapsulin samples.

Table 2. Mechanical and Thermodynamic Characteristics of Encapsulin from In Silico Nanoindentations[a]

symmetry	F^*, nN	Z^*, nm	X^*, nm	k, N/m	E_H, GPa	E_b, GPa	ΔH, Mcal/mol	ΔG, Mcal/mol	$T\Delta S$, Mcal/mol
2-fold	0.74	18.4	3.5	0.20	0.04	2.04	4.10	1.00	3.10
3-fold	0.76	22.0	6.0	0.23	0.03	1.88	3.76	0.99	2.77
5-fold	0.57	22.4	10.3	0.31	0.06	1.23 (1.71)	3.15	1.01	2.14
exp.	0.63	15.2	3.5	0.25	0.05	1.56			

[a]Critical breaking force (F^*), critical cantilever displacement (Z^*), critical indentation (X^*), the shell spring constant (k), the Young's moduli for the Hertzian-type deformation (E_H) and bending deformation (E_b), and the enthalpy change (ΔH), Gibbs free-energy change (ΔG), and entropy change ($T\Delta S$) for structural collapse transition. Results are shown per particle orientation (2-/3-/5-fold), along with the experimental results for all in vitro nanoindentations of *T. maritima* particles.

ments provide quantitative measures of the shell stiffness and breaking forces, but they lack important information about the dynamic structural changes that accompany the mechanical response of the shell to external force loading. Therefore, we utilized our multiscale computational modeling approach to nanoindentations in silico. This approach uniquely combines the all-atom Molecular Dynamics simulations of atomic structural models of biological particles and the Langevin simulations of their native-topology based Self-Organized Polymer (SOP)[33,34] coarse-grained reconstructions (see SI, Methods). We employed this approach in earlier work to explore the biomechanical properties of virus particles and microtubule polymers.[35−37] The use of high-performance computing on Graphics Processing Units (GPUs)[33,37,46] has enabled us to perform nanoindentations in silico on the millisecond time scale using the relevant experimental probe (cantilever) velocity $\nu_f = 1.0 \ \mu$m/s and cantilever tip radius R_{tip}

= 20 nm (cantilever spring constant κ = 0.05 N/m). To study the effect of particle orientation observed experimentally, we indented the encapsulin shell along the 2-, 3-, and 5-fold icosahedral symmetry axes (see Movies S1, S2, and S3). The SOP model of encapsulin is based on the crystal structure of *T. maritima* encapsulin, the only $T = 1$ encapsulin for which an atomic structure is currently available. The published structure of *T. maritima* encapsulin includes only a rather preliminary description of the cargo molecule, as only 60 short segments of the cargo-anchoring sequence are included in the model at a hypothetical cargo binding site on the shell interior. There is thus no complete and accurate information about the structure and atomic coordinates of the cargo molecule inside *T. maritima* encapsulin, which prevented us from meaningful molecular modeling of the cargo-loaded bacterial nanocompartment. For this reason, we have performed the nanoindentation in silico studies for the empty shell only. We also tested empty

T. maritima encapsulin shells by AFM experimentally, and the results obtained showed that the nanocompartments from both *T. maritima* and *B. linens* have indistinguishable spring constants, as well as critical indentations and breaking forces (see Table 1).

The experimental and simulated force−indentation spectra for cargo-free *T. maritima* encapsulin show good qualitative and quantitative agreement (Figure 3a, SI, Figure S3), in terms of the critical force F^* and critical deformation X^*, and the average slope of the FX curves k (Table 2). This remarkable agreement enabled us to interpret fine features of the FX spectra and provide a structure-based understanding of the dynamic transitions. In agreement with experiment, the simulated FX curves also show the initial nonlinear deformation regime ($X \approx 1-2$ nm). In this regime, the cantilever tip compresses the protein layer of the shell under the tip, thereby changing its local curvature and increasing the tip-shell contact area (structure **1** in Figure 3b). This is followed by the linear regime of elastic deformation for $X \approx 2.0-3.5$ nm (indention along the 2-fold symmetry axis) and for $X \approx 2.5-6.0$ nm (indentation along the 3-fold axis), which is characterized by bending of the side portions of the shell (structure **2** in Figure 3b). For $X > 3.5$ nm (2-fold symmetry) and $X > 6.0$ nm deformations (3-fold symmetry), the shell transitions to the globally collapsed state (damaged structure **3** in Figure 3b). Interestingly, when indented along the 2- and 3-fold symmetry axes the structural collapse occurs in one step, whereas for indentations along the 5-fold symmetry axis the shell exhibits two-step transitions (Figure 3c). Similar two-step transitions, which correspond to the FX spectra with double force maxima, are also observed experimentally (Figure 3d). Structural analysis revealed that at $X \approx 2.6$ nm and $F \approx 0.5$ nN the icosahedral shell first undergoes inward buckling of the vertex, but the structure continues to respond mechanically to the applied compressive force. At $X \approx 10.3$ nm and $F \approx 0.57$ nN, encapsulin undergoes the second transition which culminates in the structural collapse (snapshots in Figure 3c). Since the AFM experiment did not reveal any evidence of the 58mer complex, we performed pilot nanoindentations in silico on the encapsulin shell without a dimer to mimic a possible 58mer complex. The results obtained for the incomplete shell were similar to the 60mer complex (data are not shown). This suggests that our AFM experiments may not be able to distinguish between the two assemblies.

As we showed in our recent study,[38] the two distinctly different regimes of encapsulin's mechanical response detected in the experimental and simulated FX spectra implies the need for two Young's moduli, which fully characterize the mechanical properties of the shell in the entire range of mechanical deformation (see Supplementary Methods, SI). The Young's modulus E_H corresponds to the mechanical resistance of protein layer around the tip-shell contact area (see Figure 3a and Figure S4, SI). This Hertzian type of mechanical excitation dominates the initial weakly nonlinear regime of the FX spectra. E_H was obtained by fitting the FX curves up to $X \approx 2$ nm indentation with the Hertzian ansatz $F = \text{const } X^{3/2}$. The Young's modulus E_b corresponds to the linear force-response due to bending deformations of the side portions of encapsulin structure, which become increasingly loaded mechanically in the $X \approx 2-6$ nm interval (see Figure 3a and Figure S4, SI). Theoretical modeling of the experimental and simulated FX curves (see Supplementary Methods, SI) revealed that $E_H \approx 40-60$ MPa, whereas $E_b \approx 1.2-2.0$ GPa (Table 2). These

estimated values of the Young's moduli explain why deformation of the protein layer occurs earlier and with more ease than bending of the capsid walls. For encapsulin walls we found the Young's modulus to be of the order of a Gigapascal (from experiment and simulations), which is strikingly similar to the Young's modulus of bacteriophage HK97 procapsids and mature capsids as well as of other viral capsids (∼1−3 GPa) that, just as HK97, share the same fold of the capsid protein with encapsulins.[24−29] Moreover, the buckling transition of the vertex, observed in encapsulin, has been also found in nanoindentations in silico on HK97.[37] Despite the wide variety of morphologies, including icosahedral $T = 1, 3, 7, 16$ and prolate shells, capsids with the HK97 fold have thus far shown a remarkably consistent Young's modulus in the Gigapascal range. These results indicate that the structural similarity of encapsulin to bacteriophage capsids translates into similar mechanical properties.

Next, we calculated the enthalpy change ΔH, Gibbs free energy change ΔG, and entropy change $T\Delta S$ for structural collapse using nanoindentations along each symmetry axis (see Supplementary Methods, SI). The results show significant entropic contribution to the shell deformation ($T\Delta S = 2-3$ Mcal/mol), which is comparable yet smaller than the enthalpy change ($\Delta H = 3-4$ Mcal/mol; Table 2). As we demonstrated previously,[35−37] the entropy increase observed in the course of forced deformation is accompanied by the increase in the capsid stiffness, which occurs due to remodeling of the shell structure, whose protein subunits tend to rearrange underneath the cantilever tip. Subsequent Crooks theorem based estimation of the reversible deformation work revealed that the large ∼1 Mcal/mol free energy is required to induce structural collapse of the nanocompartment. Encapsulin is thus not only mechanically rigid, as reflected by the high elastic modulus of the shell, but also mechanically resilient and, therefore, a strikingly robust biomaterial.

■ DISCUSSION

Combining hybrid structural and biophysical approaches we here set out to probe the assembly and cargo-loading properties of encapsulins, thereby also addressing the effect of cargo-loading on the mechanical properties of the particle. From the native mass spectrometry data we learned that *B. linens* encapsulin packages solely a single copy of the native hexameric cargo enzyme DyP. With the inner volume being much larger, the DyP loading capacity of encapsulin is thus not restricted by the inner volume, but seems to depend on the shape and configuration of the cargo enzyme. In line with this hypothesis, we found earlier by native MS that encapsulin can carry up to 12 copies of monomeric GFP-like proteins, amounting to ∼400 kDa of cargo, compared to ∼240 kDa for a single DyP hexamer (a packing fraction, expressed as number of cargo molecules per available cargo binding site, of 0.2 for TFP compared to 0.1 for DyP).[15,19] Presumably, the 12 copies of the non-native cargo protein are more evenly distributed along the nanocompartment interior than the compact DyP hexamer, allowing a greater total cargo mass and volume to be encapsulated. Our data suggest that DyP cargo can also be encapsulated in incomplete 58mer encapsulin, hinting at that cargo encapsulation precedes capsid completion. Several nanocompartment subcomplexes were detected by native MS, which showed a distinct preference for even-numbered stoichiometries, suggesting an assembly pathway where the nanocompartment grows by the addition of 2-fold symmetry related dimers, with an

experimentally observed barrier for the packing of the last dimer into the final 60mer particle. Similarly, disassembly of 60mer encapsulin shells via a pathway that involves the loss of dimers could also explain the presence of the subcomplexes detected in our experiments.

We firmly established the nature of the different encapsulin particles by native mass spectrometry, allowing us to further investigate and compare their biophysical properties. Using AFM, we observed that the stiffness of the compartment is not substantially affected by cargo loading. However, the critical breaking force decreases significantly, indicating that the cargo-loaded nanocompartment becomes less stable. This effect is observed both in encapsulin carrying native or non-native cargo, indicating that binding of the anchoring peptide is largely responsible for the effect. The destabilizing effect of cargo binding could further contribute to the encapsulation of a single DyP hexamer, assuming that encapsulation of a second hexamer would render the nanocompartment so unstable that it is not sampled in the MS experiments.

The substoichiometric binding of cargo inside encapsulin poses the question of how it may result in an apparently global destabilization of the shell. We suggest that localized binding of cargo on the shell interior mechanically frustrates the shell by breaking local symmetry. Bound cargo acts like a nucleating defect for mechanical failure, thereby decreasing the breaking force, as measured in our AFM experiments. This could further explain how binding of such structurally dissimilar cargo as DyP and TFP produces such similar effects on the mechanical resilience of the shell. Following the same line of reasoning, cargo binding could produce a global structural change that relieves the local mechanical frustration as a result of cargo binding, which would similarly explain how localized cargo binding produces a global destabilization of the shell and further explain why the magnitude of the effect is the same with DyP and TFP loading, despite the difference in total cargo load. In-depth structural studies that explore the atomic-scale differences between cargo-loaded and empty encapsulin could shed light on this issue, as it would also allow systematic mechanical testing using the in silico nanoindentation approach described here. Alternatively, the destabilizing effect of cargo binding could follow a similar mechanism as recently proposed for bacteriophage P22 capsids.[47] Here, strong cargo−cargo coupling decreases the mechanical resilience of the capsid, which could also be the case for hexameric DyP, but is not expected for monomeric TFP.

Our nanoindentations in silico revealed several mechanical details that were in line with the experimental AFM data. The results of multiscale modeling indicated that the locally imposed curvature of the shell along the perimeter of the tip-particle contact site and deformation of the particle's side portions is what causes the shells to collapse under the externally applied force (see Supplementary Movies S1, S2, and S3). The observed difference in breaking force between cargo-free and cargo-loaded encapsulin therefore hints at the underlying structural difference between empty and filled compartments that makes the externally imposed curvature of the shell less easily sustained. Regardless of the cargo loading state, encapsulins are very stable and exhibit a high rigidity still resisting ~1 Mcal/mol of work before undergoing a structural collapse transition.

CONCLUSIONS

Our findings demonstrate that *B. linens* and *T. maritima* encapsulins are mechanically rigid single-enzyme nanoreactors, making them robust materials for application in engineered nanodevices. Encapsulin dimers represent stable substructures of the compartment and are therefore likely candidates as the unit of assembly. The bacterial nanocompartment mechanically behaves like the equally rigid bacteriophage particles, such as the capsid of HK97. The similarity of the fold of their capsid proteins may go a long way to explain their similar mechanical response to nanoindentation.

ASSOCIATED CONTENT

Ⓢ Supporting Information

The Supporting Information is available free of charge on the ACS Publications website at DOI: 10.1021/acs.biomac.6b00469.

> Supporting Materials and Methods and supporting Figures S1−S4 (PDF).
> Indentation of the encapsulin shell along the 2-fold icosahedral symmetry axis (AVI).
> Indentation of the encapsulin shell along the 3-fold icosahedral symmetry axis (AVI).
> Indentation of the encapsulin shell along the 5-fold icosahedral symmetry axis (AVI).

AUTHOR INFORMATION

Corresponding Authors

*E-mail: a.j.r.heck@uu.nl.
*E-mail: gwuite@nat.vu.nl.

Notes

The authors declare no competing financial interest.

ACKNOWLEDGMENTS

REFERENCES

(1) Vriezema, D. M.; Comellas Aragonès, M.; Elemans, J. A. A. W.; Cornelissen, J. J. L. M.; Rowan, A. E.; Nolte, R. J. M. *Chem. Rev.* **2005**, *105*, 1445−1489.

(2) Douglas, T.; Young, M. *Science* **2006**, *312*, 873−875.

(3) O'Neil, A.; Reichhardt, C.; Johnson, B.; Prevelige, P. E.; Douglas, T. *Angew. Chem., Int. Ed.* **2011**, *50*, 7425−7428.

(4) Patterson, D. P.; Prevelige, P. E.; Douglas, T. *ACS Nano* **2012**, *6*, 5000−5009.

(5) Comellas-Aragonès, M.; Engelkamp, H.; Claessen, V. I.; Sommerdijk, N. A. J. M.; Rowan, A. E.; Christianen, P. C. M.;

Maan, J. C.; Verduin, B. J. M.; Cornelissen, J. J. L. M.; Nolte, R. J. M. *Nat. Nanotechnol.* **2007**, *2*, 635−639.

(6) Wörsdörfer, B.; Woycechowsky, K. J.; Hilvert, D. *Science* **2011**, *331*, 589−592.

(7) Gitai, Z. *Cell* **2005**, *120*, 577−586.

(8) Yeates, T. O.; Crowley, C. S.; Tanaka, S. *Annu. Rev. Biophys.* **2010**, *39*, 185−205.

(9) Yeates, T. O.; Thompson, M. C.; Bobik, T. A. *Curr. Opin. Struct. Biol.* **2011**, *21*, 223−231.

(10) Kerfeld, C. A.; Heinhorst, S.; Cannon, G. C. *Annu. Rev. Microbiol.* **2010**, *64*, 391−408.

(11) Akita, F.; Chong, K. T.; Tanaka, H.; Yamashita, E.; Miyazaki, N.; Nakaishi, Y.; Suzuki, M.; Namba, K.; Ono, Y.; Tsukihara, T.; Nakagawa, A. *J. Mol. Biol.* **2007**, *368*, 1469−1483.

(12) McHugh, C. A.; Fontana, J.; Nemecek, D.; Cheng, N.; Aksyuk, A. A.; Heymann, J. B.; Winkler, D. C.; Lam, A. S.; Wall, J. S.; Steven, A. C.; Hoiczyk, E. *EMBO J.* **2014**, *33*, 1896−1911.

(13) Contreras, H.; Joens, M. S.; McMath, L. M.; Le, V. P.; Tullius, M. V.; Kimmey, J. M.; Bionghi, N.; Horwitz, M. A.; Fitzpatrick, J. A.; Goulding, C. W. *J. Biol. Chem.* **2014**, *289*, 18279−18289.

(14) Sutter, M.; Boehringer, D.; Gutmann, S.; Günther, S.; Prangishvili, D.; Loessner, M. J.; Stetter, K. O.; Weber-Ban, E.; Ban, N. *Nat. Struct. Mol. Biol.* **2008**, *15*, 939−947.

(15) Rurup, W. F.; Snijder, J.; Koay, M. S. T.; Heck, A. J. R.; Cornelissen, J. J. L. M. *J. Am. Chem. Soc.* **2014**, *136*, 3828−32.

(16) Moon, H.; Lee, J.; Min, J.; Kang, S. *Biomacromolecules* **2014**, *15*, 3794−3801.

(17) Tamura, A.; Fukutani, Y.; Takami, T.; Fujii, M.; Nakaguchi, Y.; Murakami, Y.; Noguchi, K.; Yohda, M.; Odaka, M. *Biotechnol. Bioeng.* **2015**, *112*, 13−20.

(18) Snijder, J.; Heck, A. J. R. *Annu. Rev. Anal. Chem.* **2014**, *7*, 43−64.

(19) Snijder, J.; van de Waterbeemd, M.; Damoc, E.; Denisov, E.; Grinfeld, D.; Bennett, A.; Agbandje-McKenna, M.; Makarov, A.; Heck, A. J. *J. Am. Chem. Soc.* **2014**, *136*, 7295−7299.

(20) Rose, R. J.; Damoc, E.; Denisov, E.; Makarov, A.; Heck, A. J. R. *Nat. Methods* **2012**, *9*, 1084−1086.

(21) Nguyen, H. D.; Reddy, V. S.; Brooks, C. L., III *Nano Lett.* **2007**, *7*, 338−344.

(22) Rapaport, D. C. *Physical Review E - Statistical, Nonlinear, and Soft Matter Physics* **2012**, *86*, 051917.

(23) Pierson, E. E.; Keifer, D. Z.; Selzer, L.; Lee, L. S.; Contino, N. C.; Wang, J. C.; Zlotnick, A.; Jarrold, M. F. *J. Am. Chem. Soc.* **2014**, *136*, 3536−3541.

(24) Roos, W. H.; Bruinsma, R.; Wuite, G. J. L. *Nat. Phys.* **2010**, *6*, 733−743.

(25) Roos, W. H.; Gertsman, I.; May, E. R.; Brooks, C. L., III; Johnson, J. E. *Proc. Natl. Acad. Sci. U. S. A.* **2012**, *109*, 2342−2347.

(26) Ivanovska, I. L.; de Pablo, P. J.; Ibarra, B.; Sgalari, G.; MacKintosh, F. C.; Carrascosa, J. L.; Schmidt, C. F.; Wuite, G. J. *Proc. Natl. Acad. Sci. U. S. A.* **2004**, *101*, 7600−7605.

(27) Hernando-Perez, M.; Miranda, R.; Aznar, M.; Carrascosa, J. L.; Schaap, I. A.; Reguera, D.; de Pablo, P. J. *Small* **2012**, *8*, 2366−2370.

(28) Smith, D. E.; Tans, S. J.; Smith, S. B.; Grimes, S.; Anderson, D. L.; Bustamante, C. *Nature* **2001**, *413*, 748−752.

(29) Roos, W. H.; Radtke, K.; Kniesmeijer, E.; Hylkje, G.; Sodeik, B.; Wuite, G. J. L. *Proc. Natl. Acad. Sci. U. S. A.* **2009**, *106*, 9673−9678.

(30) Roos, W. H. *Methods Mol. Biol.* **2011**, *783*, 251−264.

(31) Baclayon, M.; Wuite, G. J. L.; Roos, W. H. *Soft Matter* **2010**, *6*, 5273−5285.

(32) Snijder, J.; Ivanovska, I. L.; Baclayon, M.; Roos, W. H.; Wuite, G. J. L. *Micron* **2012**, *43*, 1343−1350.

(33) Zhmurov, A.; Dima, R. I.; Kholodov, Y.; Barsegov, V. SOP-GPU. *Proteins: Struct., Funct., Genet.* **2010**, *78*, 2984−2999.

(34) Hyeon, C.; Dima, R. I.; Thirumalai, D. *Structure* **2006**, *14*, 1633−1645.

(35) Kononova, O.; Snijder, J.; Brasch, M.; Cornelissen, J.; Dima, R. I.; Marx, K. A.; Wuite, G. J.; Roos, W. H.; Barsegov, V. *Biophys. J.* **2013**, *105*, 1893−1903.

(36) Kononova, O.; Kholodov, Y.; Theisen, K. E.; Marx, K. A.; Dima, R. I.; Ataullakhanov, F. I.; Grishchuk, E. L.; Barsegov, V. *J. Am. Chem. Soc.* **2014**, *136*, 17036−17045.

(37) Zhmurov, A.; Rybnikov, K.; Kholodov, Y.; Barsegov, V. *J. Phys. Chem. B* **2011**, *115*, 5278−5288.

(38) Kononova, O.; Snijder, J.; Kholodov, Y.; Marx, K. A.; Wuite, G. J.; Roos, W. H.; Barsegov, V. *PLoS Comput. Biol.* **2016**, *12*, e1004729.

(39) Rurup, W. F.; Cornelissen, J. J. L. M.; Koay, M. S. T. *Methods Mol. Biol.* **2015**, *1252*, 61−67.

(40) Van Den Heuvel, R. H. H.; van Duijn, E.; Mazon, H.; Synowsky, S. A.; Lorenzen, K.; Versluis, C.; Brouns, S. J.; Langridge, D.; van der Oost, J.; Hoyes, J.; Heck, A. J. *Anal. Chem.* **2006**, *78*, 7473−7483.

(41) Tahallah, N.; Pinkse, M.; Maier, C. S.; Heck, A. J. R. *Rapid Commun. Mass Spectrom.* **2001**, *15*, 596−601.

(42) Lorenzen, K.; Versluis, C.; van Duijn, E.; van den Heuvel, R. H. H.; Heck, A. J. R. *Int. J. Mass Spectrom.* **2007**, *268*, 198−206.

(43) Sader, J. E.; Chon, J. W. M.; Mulvaney, P. *Rev. Sci. Instrum.* **1999**, *70*, 3967−3969.

(44) De Pablo, P. J.; Colchero, J.; Gómez-Herrero, J.; Baró, A. M. *Appl. Phys. Lett.* **1998**, *73*, 3300−3302.

(45) Horcas, I.; Fernandéz, R.; Gómez-Rodríguez, J. M.; Colchero, J.; Gómez-Herrero, J.; Baro, A. M. *Rev. Sci. Instrum.* **2007**, *78*, 013705.

(46) Alekseenko, A.; Kononova, O.; Kholodov, Y.; Marx, K. A.; Barsegov, V. *J. J. Comput. Chem.* **2016**, *37*, 1537−1551.

(47) Llauró, A.; Luque, D.; Edwards, E.; Trus, B. L.; Avera, J.; Reguera, D.; Douglas, T.; De Pablo, P. J.; Castón, J. R. *Nanoscale* **2016**, *8*, 9328−9336.